Compartmentalization of antagonistic Ca^{2+} signals in developing cochlear hair cells

Marcelo J. Moglie[a], Paul A. Fuchs[b,c], Ana Belén Elgoyhen[a,d], and Juan D. Goutman[a,1]

[a]Instituto de Investigaciones en Ingeniería Genética y Biología Molecular "Dr. Héctor N. Torres," Consejo Nacional de Investigaciones Científicas y Técnicas (INGEBI–CONICET), 1428 Buenos Aires, Argentina; [b]Department of Otolaryngology-Head and Neck Surgery, Center for Hearing and Balance, The Johns Hopkins University School of Medicine, Baltimore, MD 21205; [c]Center for Sensory Biology, Institute for Basic Biomedical Sciences, The Johns Hopkins University School of Medicine, Baltimore, MD 21205; and [d]Instituto de Farmacología, Facultad de Medicina, Universidad de Buenos Aires, 1121 Buenos Aires, Argentina

Edited by Robert Fettiplace, University of Wisconsin–Madison, Madison, WI, and accepted by Editorial Board Member Jeremy Nathans January 10, 2018 (received for review November 1, 2017)

During a critical developmental period, cochlear inner hair cells (IHCs) exhibit sensory-independent activity, featuring action potentials in which Ca^{2+} ions play a fundamental role in driving both spiking and glutamate release onto synapses with afferent auditory neurons. This spontaneous activity is controlled by a cholinergic input to the IHC, activating a specialized nicotinic receptor with high Ca^{2+} permeability, and coupled to the activation of hyperpolarizing SK channels. The mechanisms underlying distinct excitatory and inhibitory Ca^{2+} roles within a small, compact IHC are unknown. Making use of Ca^{2+} imaging, afferent auditory bouton recordings, and electron microscopy, the present work shows that unusually high intracellular Ca^{2+} buffering and "subsynaptic" cisterns provide efficient compartmentalization and tight control of cholinergic Ca^{2+} signals. Thus, synaptic efferent Ca^{2+} spillover and cross-talk are prevented, and the cholinergic input preserves its inhibitory signature to ensure normal development of the auditory system.

cochlea | hair cells | synaptic transmission | calcium

Small, compact inner hair cells (IHCs) of the mammalian cochlea are responsible for converting sound information into electrical potentials for transmission to the central nervous system. However, in altricial rodents, IHCs only start to detect airborne vibrations at the end of their second postnatal week (1, 2). During these first 2 wk, animals are deaf but hair cells show rhythmic electrical activity, firing spontaneous action potentials (APs) driven by Ca^{2+} influx (3, 4). IHC spontaneous spiking is thought to be responsible for driving electrical activity throughout the entire auditory pathway (5), which is critical for the maturation and wiring of auditory circuits (reviewed in ref. 6). Moreover, the specific pattern of activity, featuring long periods of silence followed by bursts of APs with a specific temporal structure, is required for normal development (7, 8). It was recently shown that supporting cells in the developing organ of Corti play a fundamental role in establishing waves of activity (9). Some debate still exists on whether hair cells are intrinsically active and only modulated by supporting tissue (10–12) or if waves of ATP released by supporting cells are required for initiation of APs (9, 13). Each IHC is innervated by multiple spiral ganglion neurons (SGNs) making individual bouton-like contacts (14, 15). During an AP, voltage-gated Ca^{2+} channels (VGCCs) are activated and glutamate is released onto each afferent synapse (16, 17). Therefore, Ca^{2+} entering through VGCCs has a critical role in driving APs and also catalyzing vesicle fusion to the plasma membrane (Fig. 1*A*).

Besides the multiple afferent-glutamatergic synaptic boutons, developing IHCs also receive efferent-cholinergic inputs from fibers originating in the medial olivocochlear complex (MOC) (18–20) (Fig. 1*A*). The nicotinic acetylcholine receptor (nAChR) mediating this synapse is assembled from two specialized subunits, α9 and α10 (21–23), with an unusually high Ca^{2+} permeability (23, 24). Upon acetylcholine (ACh) release, Ca^{2+} influx through these receptors activates a nearby SK2, small-conductance, potassium (K^+) channel, producing a net hyperpolarization of the IHC membrane potential (20, 25). Thus, "efferent" Ca^{2+} ions are presumed to play an inhibitory role (Fig. 1*A*), which might regulate IHC excitability and modulate the pattern of AP firing (7, 10, 26). Interestingly, this cholinergic input to IHCs is present over the same time period in which animals are deaf and completely disappears a few days later (27, 28). The importance of this modulation becomes evident in animals lacking the MOC system, in which the auditory system fails to develop correctly, leading to altered connectivity maps and hearing deficits (7, 8, 29).

However, if Ca^{2+} influx through hair cell nAChRs at efferent contacts could spread and activate transmitter release at afferent synapses on diffusionally compact prehearing IHCs, the efferent system would also exert excitation on the afferent auditory pathway and provide more complex feedback. Thus, the compartmentalization and dynamics of efferent Ca^{2+} signals underlie the functional signature of efferent activity. These were now examined by recording IHC electrical activity while performing Ca^{2+} imaging experiments. Moreover, the possibility of efferent Ca^{2+} spillover and afferent excitation was evaluated by measuring activity at SGN boutons while activating cholinergic synapses. In addition, electron microscopy (EM) 3D reconstruction was used to determine the number, location, and distances between synapses. Despite the very close proximity of afferent and

Significance

Cochlear inner hair cells (IHCs) are responsible for transducing sound waves and relaying acoustic information to the brain through its afferent synapse. During development, IHCs exhibit sensory-independent activity, supported by voltage-gated Ca^{2+} influx, which is critical for the normal maturation of the auditory system. This spontaneous activity is modulated by an inhibitory cholinergic input, mediated by nicotinic receptors with unusually high Ca^{2+} permeability, leading to the activation of hyperpolarizing SK channels. Thus, Ca^{2+} should play distinct excitatory and inhibitory roles in small, compact IHCs. This work presents evidence for specialized cellular mechanisms that maintain local compartmentalization of Ca^{2+} signals and prevent synaptic cross-talk. Thus, the cholinergic input preserves its inhibitory signature to ensure normal development of the auditory system.

Author contributions: M.J.M., A.B.E., and J.D.G. designed research; M.J.M. and P.A.F. performed research; M.J.M., P.A.F., and J.D.G. analyzed data; and M.J.M., P.A.F., A.B.E., and J.D.G. wrote the paper.

The authors declare no conflict of interest.

This article is a PNAS Direct Submission. R.F. is a guest editor invited by the Editorial Board.

[1]To whom correspondence should be addressed. Email: goutman@dna.uba.ar.

This article contains supporting information online at www.pnas.org/lookup/suppl/doi:10.1073/pnas.1719077115/-/DCSupplemental.

Published online February 8, 2018.

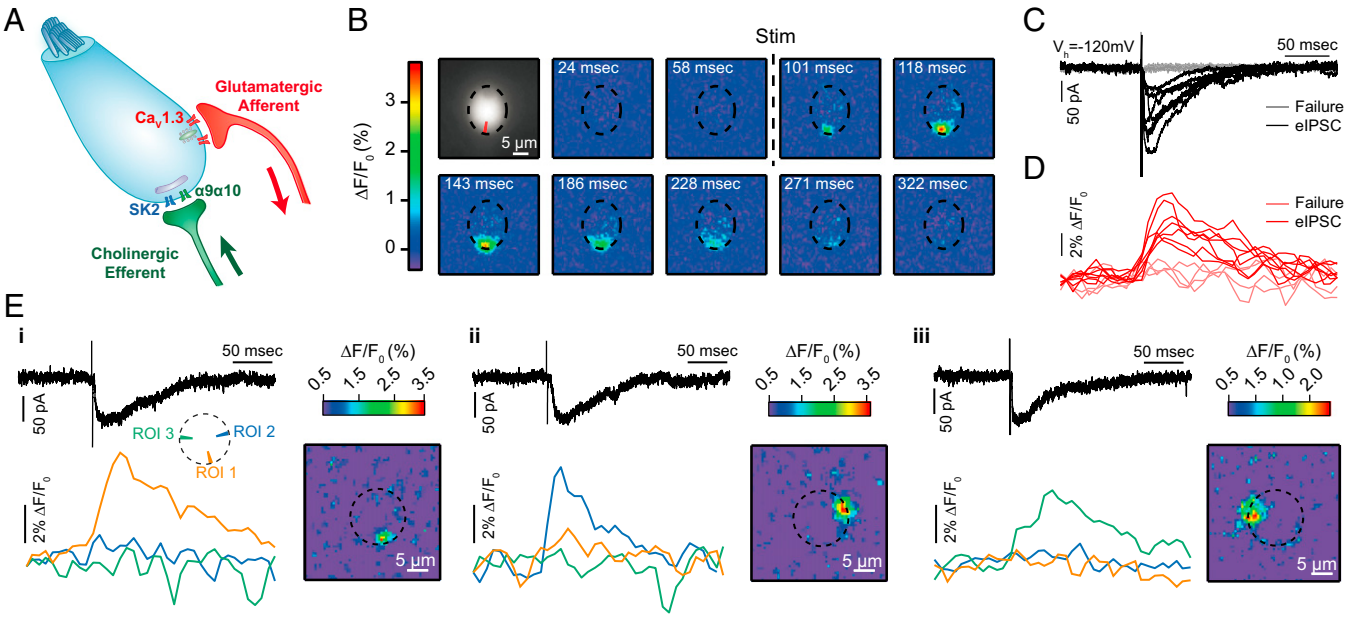

Fig. 1. Ca^{2+} signals in IHCs following efferent fiber electrical stimulation. (*A*) Schematic representation of an IHC in the postnatal developmental period previous to the onset of hearing. Both efferent cholinergic and afferent glutamatergic contacts are present at the basal pole of the IHC. (*B*) Sequence of wide-field microscopy images of an IHC filled with Fluo-4 and illuminated with 488-nm LED light during efferent electrical stimulation. "Stim" indicates when the electric stimulus was applied. The IHC base contour is outlined with a dashed line. The ROI is defined by the red shape depicted in the first image. (*C*) Representative whole-cell current traces during efferent electrical stimulation (V_h = −120 mV). Black traces represent those trials where an eIPSC was detected after the stimulus artifact (failures are shown in gray). (*D*) Fluorescence signals measured at the ROI indicated in *B* during the same trials shown in *C*. Red traces correspond to trials in *C* where an IPSC was detected, and failures are shown in pink. (*E*, *i–iii*) Representative responses activating fluorescence changes in three different portions of the IHC cytoplasm. Each panel represents a different single synaptic event. (*Top*) Black traces show the electrophysiological signal. (*Bottom*) Traces show the spatially diverse Ca^{2+} fluorescence signals measured in the radial ROIs, indicated by colors in the scheme. Images represent the peak of the Ca^{2+} signal measured for the corresponding synaptic event.

efferent contacts, Ca^{2+} signals were well segregated, preventing efferent-to-afferent synaptic cross-talk. Diffusible and fixed Ca^{2+} buffering systems, likely to include the IHC postsynaptic cistern apposed to efferent fibers, prevent extensive diffusion of Ca^{2+} ions during the physiological operation of this synapse. Thus, during the critical auditory developmental period, efferent fibers only exhibit an inhibitory role on AP firing.

Results

Synaptic Ca^{2+} Signals in IHCs Following Efferent Fiber Electrical Stimulation. During development, cochlear IHCs receive a transient cholinergic innervation from MOC fibers mediated by the highly Ca^{2+}-permeable α9α10 nAChR (23, 24). Using the high-affinity fluorescent Ca^{2+} indicator Fluo-4 (0.4 mM), low intracellular buffering (0.5 mM EGTA), and large driving force for Ca^{2+} [IHC holding membrane potential (V_h) = −120 mV], it was possible to detect changes in fluorescence due to Ca^{2+} influx during single synaptic events. Fig. 1*B* shows a representative sequence of images where a transient Ca^{2+} increase can be seen in a specific region of the IHC basal pole following single-pulse efferent fiber stimulation. Traces in Fig. 1*C* represent inhibitory postsynaptic currents (IPSCs) evoked by the release of ACh from efferent terminals in postnatal day 9 (P9)–P11 mice. Efferent synaptic currents are inhibitory because Ca^{2+} influx is coupled to the activation of nearby SK2 channels (20, 25). In these experimental conditions, due to the negative holding potential, currents were inward through both the α9α10 receptors and SK2 channels. Traces corresponding to synaptic failures in these experimental conditions represented 28.2 ± 4.8% of stimulation trials (Fig. 1 *C* and *D*, gray and pink traces).

The amplitude and time course of the transient changes in fluorescence were quantified by measuring the intensity at specific regions of interest (ROIs). ROIs were drawn across the IHC cytoplasm in a circular array (ROI design scheme is discussed in *Methods*) (Fig. 1*D* and Fig. S1). The average amplitude of optically detected events was 5.6 ± 0.6 $(F - F_0)/F_0$ ($\Delta F/F$, %) (n = 7 cells, n = 30–80 sweeps per cell), with an average decay time (τ_{decay}) of 135 ± 10 ms (Table S1). The IPSC average amplitude in the same set of events was 80.1 ± 5.4 pA, with a τ_{decay} of 53 ± 6 ms. Fluorescence changes were also measured during synaptic failures, obtaining an average of 0.5 ± 0.1 $\Delta F/F_0$ (%) (n = 7 cells) (Table S1). Using threshold criteria (*Methods*), we were able to detect an increase in Ca^{2+} signal in only 44.0 ± 4.1% of all the trials where an evoked IPSC (eIPSC) was detected (Table S1).

Interestingly, on many occasions (≈40%), multiple regions of an IHC showed an increase in fluorescence during single efferent-cholinergic synaptic events. On average, 2.6 ± 0.2 (n = 7 cells, range: 2–3) localized Ca^{2+} hotspots were detected in each cell on a single focal plane. A representative example of the activation of multiple domains within a single IHC is shown in Fig. 1*E*: Three different regions of the cell showed independent Ca^{2+} transients during repetitions of the same stimulation protocol. These results are compatible with the activation of multiple efferent synapses located in different regions of a single cell.

Three-Dimensional Distribution of Afferent and Efferent Ca^{2+} Entry Sites. The presence of multiple Ca^{2+} hotspots was investigated further throughout the entire IHC. To this end, swept-field confocal microscopy provided confocal sections of IHCs at high rates (110 frames per second). The location of cholinergic Ca^{2+} entry sites was determined by applying short trains of shocks (four stimuli at 80 Hz, V_h = −120 mV) to produce reliable activation of efferent terminals (Fig. 2*A*). Similarly, application of a brief depolarizing pulse (V_h = −30 mV, 20 ms), leading to Ca^{2+} entry through VGCCs, revealed afferent-glutamatergic synapse locations on the same IHC (Fig. 2*B*). In

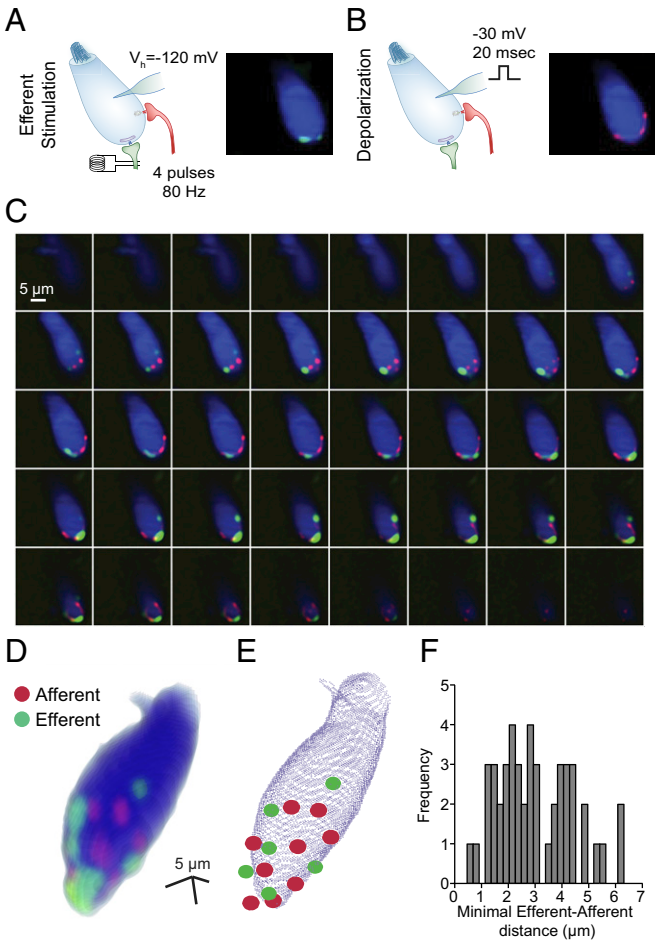

Fig. 2. Three-dimensional reconstruction of functional IHC Ca^{2+} domains using swept-field confocal microscopy. (*A*, *Left*) Scheme depicting the stimulation protocol used for imaging efferent Ca^{2+} entry sites (50 ms, 80-Hz electrical stimulation of efferent axons). (*A*, *Right*) Single Z-plane of an IHC illuminated at 488 nm and loaded with Fluo-5F and 10 mM EGTA. Cell fluorescence at rest is represented in blue to indicate location. Green hotspots represent Ca^{2+} domains at the peak of efferent stimulation. (Scale bar: 5 μm.) (*B*, *Left*) Scheme depicting the depolarization protocol to detect Ca^{2+} entry hotspots through VGCCs. (*B*, *Right*) Similar to *A*, but Ca^{2+} hotspots due to VGCC activation are represented in red. (Scale bar: 5 μm.) (*C*) Montage of peak Ca^{2+} signals in different Z-planes obtained during the protocols described in *A* and *B*. (*D*) Three-dimensional reconstruction performed with the Z-stack of images in *C*. (*E*) Representation of the same IHC illustrated in *C*. Red and green circles pinpoint the center of the afferent and efferent hotspots, respectively. (*F*) Frequency histogram of distances from each efferent hotspot in a given cell to its closest afferent hotspot.

this set of experiments, lower affinity Ca^{2+} indicator (Fluo-5F, K_d = 2.3 μM) was combined with 10 mM EGTA in the intracellular solution to minimize the spread of the Ca^{2+} signal after each stimulus and enhance the ability to identify single entry sites. Both stimulation protocols were repeated at each focal section to later construct a 3D map of synapse location within a single IHC (Fig. 2 *C* and *D*). In contrast to the hotspots detected in single focal planes (Fig. 1), there was an average of 5.9 ± 0.6 efferent cholinergic hotspots (n = 8 cells, range: 3–8 hotspots per cell) and 7.6 ± 0.4 afferent voltage-dependent Ca^{2+} entry sites per IHC (n = 8 cells, range: 6–9 afferent hotspots per cell) (Fig. 2*E*).

The location and number of Ca^{2+} entry sites through afferent synapses were confirmed by using a RIBEYE-binding peptide labeled with rhodamine (Fig. S2*A*), which is known to specifically label ribbons in retinal bipolar cells and hair cells from the cochlea (30, 31). This fluorescently labeled peptide was introduced in the cells through a patch pipette together with the Fluo-5F indicator. The peptide signal was detected in 7.5 ± 0.7 puncta per cell, showing colocalization with afferent Ca^{2+} entry in 90 ± 3% of all sites (n = 8 cells, n = 60 RIBEYE spots) (Fig. S2). On the other hand, an afferent Ca^{2+} spot without a corresponding ribbon presence was obtained in only 14 ± 3% of the cases (n = 8 cells, n = 61 afferent spots).

A minimal-maximal stimulation protocol was used to obtain an additional assessment of the number of functional efferent synapses on a single IHC. IPSCs were activated in IHCs with electrical shocks to the efferent axons of increasingly higher intensity, in steps of 10 μA. As shown in Fig. S3, an estimation of 4.4 ± 0.7 (range: 2–8, n = 8 cells) distinct efferent inputs was obtained.

Finally, the distance between functionally active glutamatergic and cholinergic synapses was determined using the swept-field confocal 3D reconstructions (Fig. 2 *D* and *E*). The mean distance of each cholinergic hotspot to its nearest glutamatergic hotspot was 3.00 ± 0.20 μm (range: 0.46–6.17 μm, n = 47 efferent-afferent pairs, n = 8 cells) (Fig. 2*F*). The minimal distance encountered between a pair of afferent and efferent hotspots in each IHC was 1.45 ± 0.25 μm (range: 0.46–2.61 μm, n = 8 cells). Similarly, the average distance from each efferent hotspot to the nearest RIBEYE puncta was 3.02 ± 0.22 μm (n = 47 efferent-RIBEYE pairs), and the minimal distance between these pairs found in each cell was 1.83 ± 0.50 μm (n = 8 cells).

Synaptic Architecture of Young IHCs. The number of efferent and afferent synapses and distances between synapses were investigated further with EM and 3D reconstruction of IHCs from young (P9) rats. A montage of ∼10 images at a magnification of 30,000× was assembled for each of (approximately) 100 serial sections to reconstruct a hair cell with sufficient resolution to ensure that all synaptic details were observed. Efferent contacts were counted if a postsynaptic cistern was present. Cisterns aligned with efferent terminals, covering approximately half of the presynaptic area, and always corresponded with the clustering of vesicles near the plasma membrane of the presynaptic terminal. The attachment of the cistern to the hair cell plasma membrane ranged from 0.5 to 1.0 μm in maximum extent.

Afferents were clearly distinguished from efferent endings by the relative lack of small vesicles, less dense cytoplasm, and association with presynaptic vesicles clustered at the hair cell membrane, with or without a visible ribbon. Individual afferent contacts could be associated with more than one ribbon, as well as several "ribbonless" vesicle clouds.

Afferent and efferent endings intermingled on the synaptic pole of the IHC, at or below the level of the nucleus (Fig. 3 *B*–*D*). Ribbons were small, 100 nm or less in width, but associated with large numbers of synaptic vesicles, both close to and extending away into the cytoplasm. There was a large number of both efferent and afferent synapses on each of three reconstructed IHCs, with up to 34 efferent cisterns associated with vesiculated efferent boutons and 25 ribbons associated with afferent contacts. On average, there were 25.3 ± 5.2 (range: 15–32, n = 3 cells) cisterns and 17.0 ± 3.8 (range: 11–24, n = 3 cells) ribbons per cell. Some efferent cisterns and synaptic ribbons were immediately adjacent (Fig. 3*A*), showing an average minimal distance of 1.57 ± 1.09 (SD) μm (range: 0.09–4.22 μm, 83 cisterns and 64 ribbons in three IHCs). However, there was a tendency for each type of synapse to cluster together. Approximately 45% of all of the identified afferent synapses were less than 1 μm from another afferent synapse, whereas 83% of efferent synapses were within 1 μm of the nearest efferent contact.

Despite differences in absolute numbers, results from Figs. 1–3 and Figs. S2 and S3 point to the presence of multiple efferent

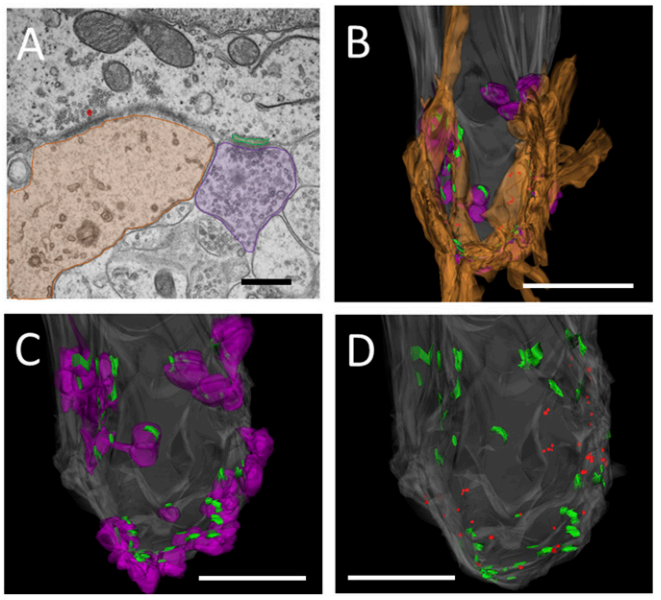

Fig. 3. Synaptic contacts on a P9 rat IHC. (*A*) Example of neighboring afferent and efferent synaptic contacts. The afferent bouton is shaded in brown, the ribbon is colored red, the efferent bouton shaded in purple, and the synaptic cistern is colored green. (Scale bar: 500 nm.) (*B–D*) Reconstruction of the IHC from a P9 rat cochlea. This cell had 19 afferent and 37 efferent contacts, associated with 25 ribbons and 37 cisterns. (*B*) Hair cell (gray) with afferents (brown), efferents (purple), ribbons (red), and cisterns (green). (Scale bar: 5 μm.) (*C*) Hair cell with efferent and cisterns only. (Scale bar: 2.5 mm.) (*D*) Hair cell with cisterns and ribbons only. (Scale bar: 2.5 μm.)

and afferent synapses within a small volume. This intimate localization of Ca^{2+} domains serving opposing roles suggests Ca^{2+} entering through efferent synapses could potentially spill over and spread to afferent release sites in developing IHCs. This possibility was evaluated further, performing repetitive stimulation of efferent inputs.

The Amplitude and Distribution of Efferent Ca^{2+} Signals Depend on Stimulation Rate. Cholinergic inhibition to IHCs during development facilitates with repetitive activation of efferent axons, enhancing its effect (32). Thus, the amplitude and distribution of Ca^{2+} signals were measured during repetitive trains of stimuli at 5, 20, and 80 Hz for 3 s. Fig. 4*A* shows representative electrophysiological traces and fluorescence signals obtained on a given IHC for each stimulation frequency. The fluorescence peak was always reached at the end of the stimulation protocol for 20- and 80-Hz trains, whereas at 5 Hz, the timing of the maximal response varied within the stimulation period, and was usually coincident with the largest eIPSC. Higher stimulation frequencies resulted in higher maximal fluorescence: 13 ± 3, 144 ± 23, and 221 ± 34 $\Delta F/F_0$ (%), respectively, for trains at 5, 20, and 80 Hz ($n = 7$ cells; Friedman's test, $P < 0.01$) (Fig. 4 *A–C*). The amplitude of the fluorescence signals correlated with the integral of the electrophysiological responses and showed no signs of Ca^{2+} indicator saturation (Spearman correlation, $P < 0.0001$) (Fig. 4*D*).

The spread of Ca^{2+} across the cytoplasm during repetitive stimulation was estimated by plotting fluorescence intensity as a function of time and ROI number (Fig. 4*B*). The coefficient of variation of fluorescence intensity (CV) across ROIs was calculated at the time point when the signal reached its maximum. Clearly defined Ca^{2+} transients were observed during 5-Hz trains, showing strong localization and heterogenous spatial distribution (Fig. 4 *B*, *i*), resulting in a CV of 0.51 ± 0.13 ($n =$ 7 cells) (Fig. 4*F*). Higher frequency trains resulted in large and uniform Ca^{2+} increases observed across all ROIs (Fig. 4 *B*, *ii* and *iii*). Consequently, significantly smaller CV values of 0.11 ± 0.02 ($n = 7$ cells) and 0.09 ± 0.01 ($n = 7$ cells) were obtained for 20 and 80 Hz, respectively (Friedman's test, $P < 0.01$) (Fig. 4*F*). It is important to mention that in the course of the 3-s trains shown in Fig. 4, synaptic responses exhibited strong depression. This observation was quantified in Fig. S4 as the ratio between the average amplitude in the last 0.5 s of the train and the maximal amplitude obtained for each frequency of stimulation. For 80-Hz trains, this ratio was 0.04 ± 0.01, whereas at 20 and 5 Hz, it was 0.19 ± 0.04 and 0.45 ± 0.10, respectively. These results indicate that extending the duration of the trains would not produce larger Ca^{2+} influx when stimulating at high frequencies.

In the past, experiments using exogenous applications of cholinergic agonists (instead of the present synaptically evoked release) have shown an extended increase in fluorescence

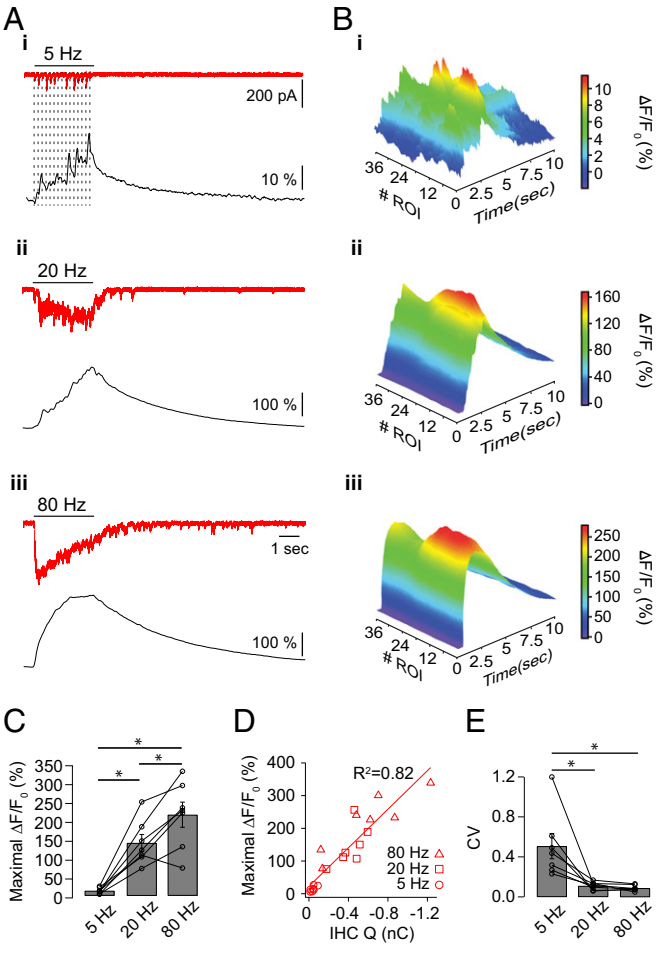

Fig. 4. Ca^{2+} influx produced by trains of efferent stimuli. Cells loaded with Fluo-4 (400 μM) and EGTA (500 μM) were imaged on a wide-field microscope using 488-nm LED illumination during efferent electrical stimulation protocols. (*A*) Representative synaptic responses (red traces) and changes in fluorescence [black traces, expressed as $\Delta F/F_0$ (%)] produced in an IHC during a 3-s electrical stimulation of efferent fibers at 5 Hz (*i*), 20 Hz (*ii*), and 80 Hz (*iii*). (*B*) Three-dimensional representation of the fluorescence signal [$\Delta F/F_0$ (%)] as a function of ROI number and time during electrical stimulation of efferent axons at 5 Hz (*i*), 20 Hz (*ii*), and 80 Hz (*iii*). (*C*) Maximal $\Delta F/F_0$ (%) reached during 5-, 20-, and 80-Hz stimulation trains. Friedman's test, $^*P < 0.01$. (*D*) Correlation between the maximal fluorescence signal and the charge (Q) accumulated at the end of the stimulation protocol (integral of synaptic currents) Spearman correlation, $P < 0.0001$. (*E*) Fluorescence CV across ROIs at the time point when the Ca^{2+} peak was reached. Friedman's test, $^*P < 0.01$.

throughout the hair cell cytoplasm (33, 34). For comparison with those earlier studies, Ca^{2+} signals were obtained from IHCs after the local application of the nAChR agonist ACh (at 10, 100, and 300 μM) (Fig. S5). In contrast to those studies, attention was focused on the Ca^{2+} transients generated in the basal pole of the cells, where synaptic contacts concentrate. At 10 μM, ACh elicited a maximal fluorescence signal similar to that observed during a 5-Hz electrical stimulation [22 ± 3 $\Delta F/F_0$ (%), n = 5 cells; Kolmogorov–Smirnov test, P = 0.37]. However, sharp peak Ca^{2+} transients, as seen with electrical stimulation, were not found. At 100 μM and 300 μM, ACh evoked very robust Ca^{2+} responses [397 ± 47 and 494 ± 115 $\Delta F/F_0$ (%), respectively; n = 5 cells] that nearly tripled the fluorescence signals measured during 80-Hz trains of electrical stimulation and presented a homogeneous distribution (CV = 0.06 ± 0.01 at 300 μM ACh, n = 5 cells) (Fig. S5 *C* and *D*).

These results indicate that upon intense activation of the efferent cholinergic input, there is a large Ca^{2+} influx into the IHC, leading to major changes in Ca^{2+} concentration throughout the cytoplasm. Thus, during sustained activity of the efferent MOC system, cross-talk between inhibitory (efferent) and excitatory (afferent) synapses is a possible scenario.

Synaptically Evoked Efferent Ca^{2+} Entry Is Not Sufficient to Evoke Afferent Glutamate Release. To examine the possibility of efferent-to-afferent synaptic cross-talk, whole-cell recordings from SGN terminals at their point of contact with the IHC were made while making local ACh applications (Fig. 5). Since the IHC intracellular milieu remained unperturbed, this experiment provided a functional assessment of the spread of the efferent Ca^{2+} signal within an intact IHC. Recordings in afferent boutons of SGNs typically present low and variable spontaneous activity during the prehearing developmental stage (17). Without IHC stimulation, the rate of excitatory postsynaptic currents (EPSCs) was 0.48 ± 0.13 s^{-1}, with a range between 0.12 and 0.85 s^{-1} (n = 7 boutons) (Fig. 5*E*). Fig. 5*A* shows a representative bouton recording with spontaneous EPSCs, showing variable amplitudes and averaging 132.5 ± 20.8 pA (n = 7 boutons). When high K^+ (25 mM) was applied in the extracellular solution, a robust increase in EPSC frequency was observed due to IHC depolarization (10.26 ± 3.56 s^{-1}, range: 0.73–24.09, n = 7 boutons) (Fig. 5 *B* and *E*). Application of 100 μM ACh produced no significant increase in the EPSC rate compared with spontaneous activity (2.63 ± 1.75 s^{-1}, range: 0.12–13.00, n = 7 boutons; Kruskal–Wallis test, $P > 0.05$). However, upon 300 μM ACh application, a robust increase in the frequency of EPSCs was obtained, with an average value of 7.40 ± 2.40 s^{-1} (range: 0.13–16.13, n = 6 boutons; Kruskal–Wallis test, $P < 0.05$) (Fig. 5 *C* and *E*). To further confirm that the effect of ACh was mediated by α9α10 nAChRs, 1 μM strychnine, a specific antagonist of the hair cell cholinergic response (23), was coapplied with 300 μM ACh. Under these conditions, EPSC rates were similar to resting levels (0.93 ± 0.39 s^{-1}, range: 0.2–2.07, n = 5 boutons; Kruskal–Wallis test, $P >$ 0.05) (Fig. 5 *D* and *E*).

At the end of each bouton recording, a second electrode was used to record from the presynaptic IHC and verify that the locally applied ACh activated a cholinergic response (Fig. 5 *C* and *D*, *Insets*). Experiments were only taken into account if both SGN and the IHC recordings were successfully performed. As shown in Fig. 5 *F* and *G*, 100 μM ACh produced IHC inward currents with an average amplitude of 388.1 ± 99.3 pA and an integral of 3.57 ± 0.99 nC (n = 7 cells), whereas a maximum of 745.6 ± 165.3 pA and 8.90 ± 1.61 nC (n = 6 cells) was obtained with 300 μM ACh. These latter responses were partially blocked in the presence of strychnine, reaching amplitudes of 321.4 ± 88.0 pA and an integral of 3.45 ± 1.09 nC (n = 5 cells) (≈45% inhibition).

These results suggest that under our experimental conditions, Ca^{2+} ions entering through α9α10 receptors activated by exogenously applied ACh can trigger the release of glutamate-filled vesicles from nearby ribbon synapses. To determine if synaptic gating of Ca^{2+} influx under physiological conditions could have this same effect, the activity of afferent boutons was monitored

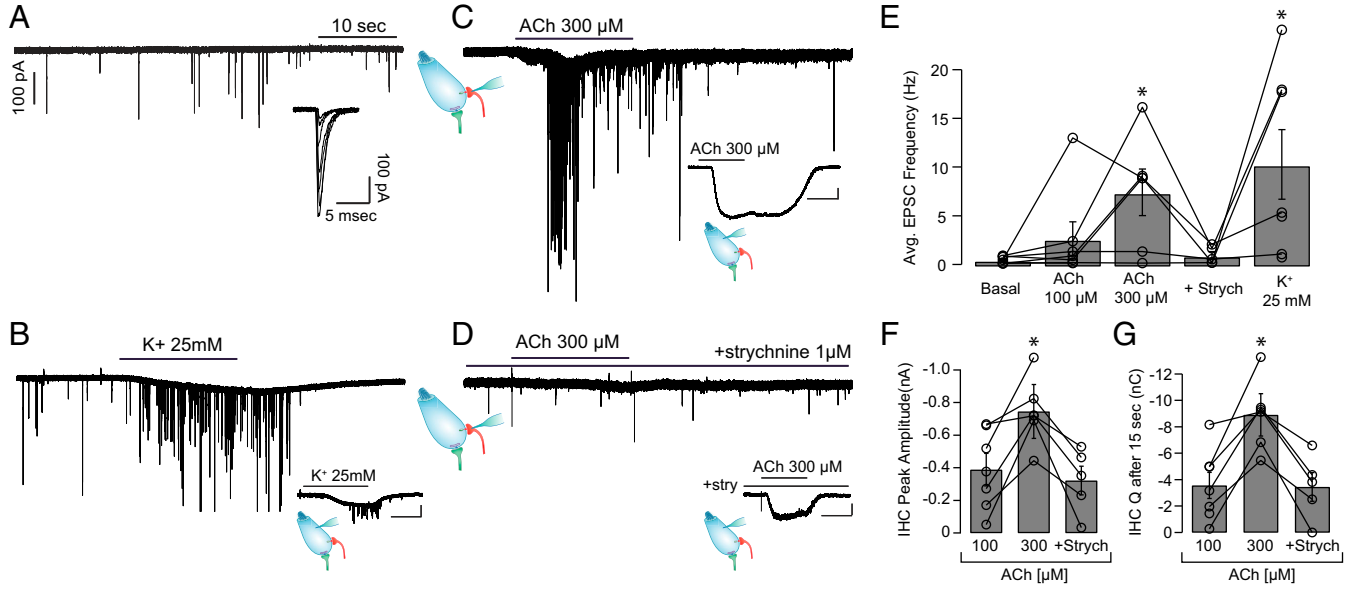

Fig. 5. Local ACh application produces an increase in the afferent EPSC rate. (*A*) Representative whole-cell recording of an afferent bouton with spontaneous EPSCs (5.8 mM K^+). (*Inset*) Detail of superimposed EPSC traces. (*B*) Bouton recording upon application of 25 mM K^+ in the extracellular solution. (*Inset*) Voltage-clamp recording from the IHC that lays presynaptic to the bouton. Representative bouton recordings during local application of 300 μM ACh (*C*) and 300 μM ACh + 1 μM strychnine (*D*) are shown. (*Insets*) IHC cholinergic currents upon application of 300 μM ACh in the absence (*C*) or presence (*D*) of 1 μM strychnine (note: IHC recordings were obtained from the cells presynaptic to the bouton shown in each panel). (Scale bars: *Insets*, 100 pA, 10 s.) (*E*) Average (Avg.) EPSC activation rate recorded in boutons during drug applications (calculated up to the end of the perfusion). Strych, strychnine. Kruskal–Wallis test, *$P < 0.05$. (*F*) Amplitude of ACh responses in IHCs. (*G*) IHC charge (Q) accumulated after 15 s of ACh application. Kruskal–Wallis test, *$P < 0.05$.

while electrically stimulating efferent fibers. As indicated in Fig. 5, under these experimental conditions, the IHC intracellular milieu also remained undisturbed. Efferent-to-afferent synaptic cross-talk was evaluated by stimulating efferent axons for 3 s at three different frequencies: 5, 20, and 80 Hz. As will be shown later, efferent stimulation at low frequencies allowed continued IHC firing (at the end of sparsely occurring synaptic potentials; see Fig. 7*A*), whereas higher frequencies suppressed firing but produced a rebound of activity at the end of the efferent train. Therefore, the following set of experiments was performed in the presence of the L-type Ca^{2+} channel blocker isradipine to prevent the entry of Ca^{2+} through VGCCs during AP firing by the IHC (35), which could lead to misinterpretations of the afferent recordings activity. The spontaneous rate of EPSCs during the application of isradipine was 0.18 ± 0.06 s^{-1} (n = 6 boutons) (Fig. 6*A*).

As shown in Fig. 6 *B* and *D*, there was no increase in EPSC rate during efferent shocks at 5 and 20 Hz for 3 s. The average EPSC activation rate was 0.17 ± 0.11 s^{-1} during the 5-Hz efferent stimulation and 0.33 ± 0.172 s^{-1} when stimulated at 20 Hz (n = 6). For 80-Hz shock trains, five of six recordings showed no alteration in EPSC activity, with a global average rate of 1.22 ± 1.16 s^{-1}. Similar to experiments in Fig. 5, after completing the SGN bouton recording, a fresh electrode was used to record from the contacting IHC and evaluate efferent synaptic responses with the same stimulating parameters (position of the stimulating electrode, intensity, and frequencies) that were used for the bouton experiments. Responses to such stimuli are shown in Fig. 6 *A–C*, *Insets*. The peak amplitude and total charge for efferent responses were significantly higher at 80 Hz (836 ± 206 pA and 1.67 ± 4.73 nC) than at 20 Hz (557 ± 108 pA and 1.02 ± 0.20 nC) and 5 Hz (183 ± 40 pA and 0.11 ± 0.33 nC) (n = 6; Friedman's test, $P < 0.05$). In accordance with previous results (36), isradipine produced a strong increase in efferent release probability, reaching an accumulated charge almost ninefold larger than that obtained in the absence of the L-type channel antagonist (Kruskal–Wallis test, $P < 0.05$) (compare Figs. 6*F* and 7*D*). In one of six recordings (identified with red triangles in Fig. 6 *D–F*), an increase in the EPSC activation rate was observed when efferents were stimulated at 80 Hz (from 0.2 to 7.0 s^{-1}) (Fig. S6). The efferent synaptic response of the IHC presynaptic to this bouton presented the highest accumulated charge: 3.6 nC (twofold larger than the average in Fig. 6*F* and 22-fold larger compared with the average in Fig. 7*D*).

Interestingly, whereas local ACh applications were successful in eliciting synaptic "cross-talk," electrical efferent stimulation failed to produce changes in most experiments, even when stimulating at a high frequency (80 Hz) and considering the isradipine-mediated potentiation of the efferent response (and, presumably, Ca^{2+} influx into the IHC). This sharp difference can be attributed to the significantly larger charge that flowed in the cells during ACh applications compared with electrical stimulations (compare Figs. 5*G* and 6*F*), despite comparable peak current amplitudes (Figs. 5*F* and 6*E*). This suggests that a stronger Ca^{2+} load than that resulting from efferent synaptic activity is required to evoke glutamate release at the IHC-afferent synapse. Thus, very efficient IHC cellular processes must operate to guarantee Ca^{2+} compartmentalization and prevent efferent/afferent cross-talk during physiological efferent activation. These could include structural diffusional barriers such as the IHC subsynaptic cisterns apposed to efferent synapses (Fig. 3), presumably also operating as Ca^{2+} sinks; strong Ca^{2+} buffering; and/or a low activation rate of efferent fibers.

Cisternal Ca^{2+} Uptake and Strong Intracellular Buffering Restrict Diffusion. First, the contribution of endoplasmic Ca^{2+}-ATPases to the process of Ca^{2+} clearance during efferent activation was evaluated using the membrane-permeant inhibitor cyclopiazonic acid (CPA) (37) and imaging cytoplasmic Ca^{2+} during brief train stimulation. Fig. 8*A* shows representative Ca^{2+} transients evoked by 10-shock trains at 5, 20, and 80 Hz, either in control conditions or after a 7-min application of CPA in the bath. No differences were found in the maximal amplitude of electrophysiological responses (control vs. CPA: 5 Hz = 94.7 ± 13.0/98.0 ± 15.3 pA, 20 Hz = 125.6 ± 13.2/140.4 ± 26.2 pA, 80 Hz = 320.9 ± 50.7/266.58 ± 49.0 pA) or Ca^{2+} transient peaks (control vs. CPA: 5 Hz = 26.6 ± 3.8/42.2 ± 6.9 ΔF, 20 Hz = 48.5 ± 8.0/68.3 ± 16.0 ΔF, 80 Hz = 110.4 ± 23.7/106.2 ± 36.3 ΔF) during efferent stimulation trains before and after CPA perfusion (n = 6;

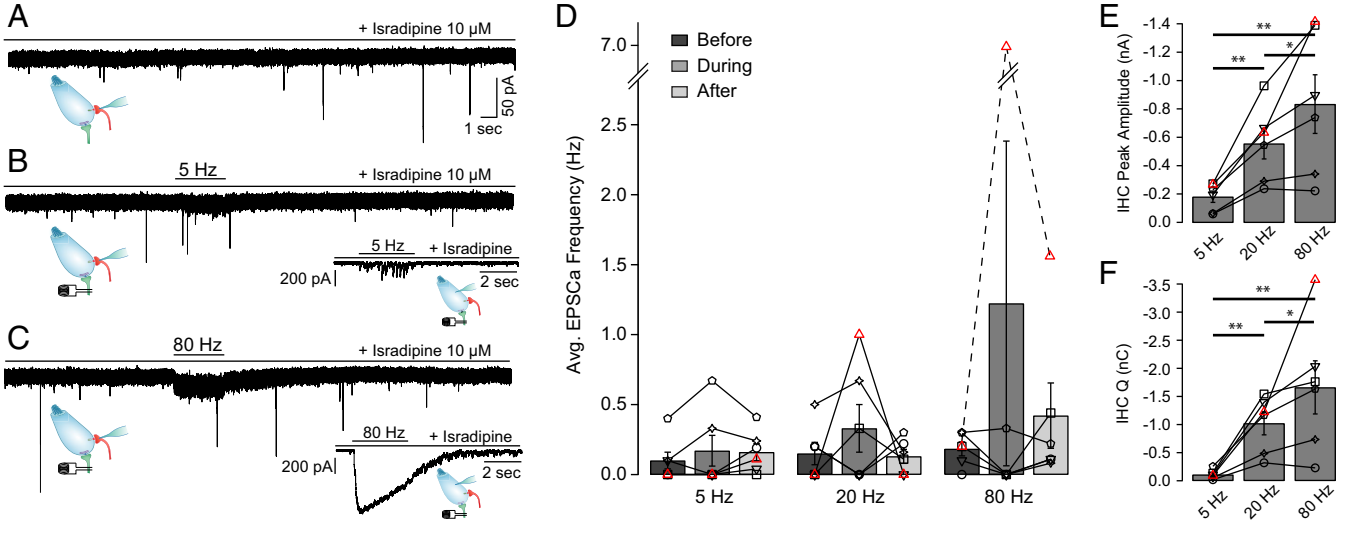

Fig. 6. Efferent electrical stimulation does not produce a rise in afferent synaptic activity. (*A*) Representative intracellular recordings of an afferent bouton in the presence of 10 μM isradipine. (*B* and *C*) Same as in *A* but during electrical stimulation of efferent fibers at 5 Hz (*B*) and 80 Hz (*C*). (*Inset*) Voltage-clamp recordings from the IHC presynaptic to the bouton. Stimulation of efferent fibers produced cholinergic synaptic currents. (*D*) Average (Avg.) EPSC rate before, during, and after efferent train stimulations at 5, 20, and 80 Hz. Each symbol represents a single bouton-IHC pair experiment. Friedman's test, $P > 0.05$. (*E*) Maximal synaptic current amplitude measured in the IHC during train stimulation. Friedman's test: $^*P < 0.05$; $^{**}P < 0.01$. (*F*) Charge (Q) accumulated at the end of the 3-s efferent train protocol at each stimulation frequency. Friedman's test: $^*P < 0.05$; $^{**}P < 0.01$.

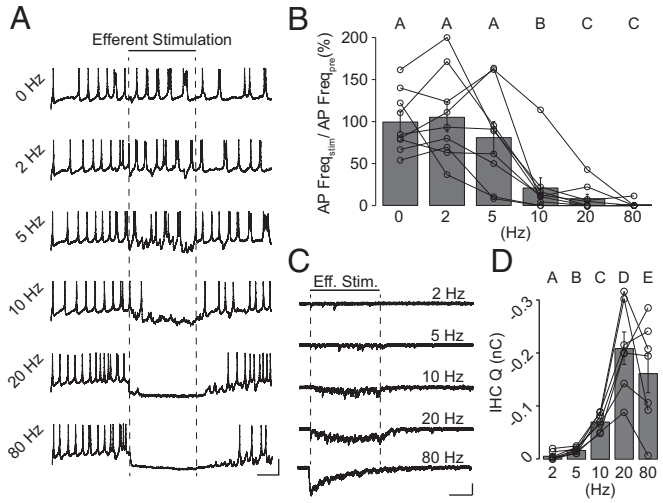

Fig. 7. Efferent train stimulation inhibits IHC AP firing. (*A*) Representative current-clamp recordings from an IHC during a short burst of APs. A 10-pA steady current was applied to trigger firing. Efferent fibers were electrically stimulated at different frequencies during the time indicated by dashed lines. (Scale bars: 20 mV, 1 s.) (*B*) Average rate of AP firing during efferent stimulation (AP $Freq_{stim}$). Values were normalized to the rate obtained during the prestimulation period (AP $Freq_{pre}$). Different uppercase letters (A–C) represent statistical differences between frequencies, Friedman's test, $P < 0.05$. (*C*) Representative voltage-clamp recordings from the same IHC in *A* during efferent stimulation (Eff. Stim.) at different frequencies. The timing of efferent stimulation is indicated by dashed lines. (Scale bars: 100 pA, 1 s.) (*D*) Charge (Q) at the end of the 3-s efferent train protocol at each stimulation frequency. Different letters (A–E) represent statistical differences between frequencies. Friedman's test, $P < 0.05$.

Friedman's test, $P > 0.05$). However, a strong lengthening of cytoplasmic Ca^{2+} τ_{decay} was observed (Fig. 8*B*), such that average 20–80% τ_{decay} increased from 1,304 ± 270, 956 ± 92, and 861 ± 160 ms at 5, 20, and 80 Hz, respectively, to 1,942 ± 235, 2,195 ± 255, and 2,137 ± 266 ms when CPA was added ($n = 6$ cells; Friedman's test, $P < 0.05$). These results indicate that an active Ca^{2+} transport mechanism mediated by cistern Ca^{2+}-ATPases contributes to shortening Ca^{2+} spread in IHC cytoplasm.

The level of intracellular Ca^{2+} buffering that could limit efferent Ca^{2+} cross-talk was estimated by measuring the coupling between SK2 channels and α9α10 receptors during efferent synaptic transmission. As SK2 activation is purely dependent on Ca^{2+}, it is a good proxy for Ca^{2+} concentration near α9α10 nAChRs (25, 28). IHCs were recorded in the perforated-patch configuration to prevent washout of endogenous buffers, and efferent fibers were electrically stimulated as previously indicated. For these experiments, the IHC holding potential was set to −40 mV, where the bulk of the membrane current is outward due to activation of SK2 channels (20, 38) (Fig. 8*C*). Additionally, IHCs were recorded in the whole-cell configuration while dialyzing their cytoplasm with different Ca^{2+} buffers: 0.5, 5 mM EGTA and 0.2, 2 mM 1,2-bis(2-aminophenoxy)ethane-*N*,*N*,*N*′,*N*′-tetraacetic acid (BAPTA). The amplitude, charge, and half-width (HW) of the SK2 currents were analyzed (Fig. 8 *D*–*F*).

As can be observed in Fig. 8*D*, the total SK2 component charge decreased with increasingly higher exogenous buffering: 2.2 ± 0.1 pC in 0.5 mM EGTA ($n = 7$), 2.1 ± 0.2 pC in 5 mM EGTA ($n = 8$), 1.9 ± 0.2 pC in 0.2 mM BAPTA ($n = 7$), and 1.2 ± 0.1 pC in 2 mM BAPTA ($n = 7$). Perforated-patch (1.3 ± 0.1 pC, $n = 5$) and 2 mM BAPTA values were similar and significantly different from the rest (Kruskal–Wallis test, $P < 0.05$). Similar to charge estimates, no statistically significant differences were found between 2 mM BAPTA and perforated-patch conditions when comparing the IPSC duration measured as the HW (Fig. 8*F*) (Kruskal–Wallis test, $P > 0.05$). As IPSC parameters are dependent on efferent release probability (32), the synaptic quantum content (m) in each experimental condition was estimated using the failures method (39). No statistical differences were found in m (Kruskal–Wallis test, $P > 0.05$), indicating similar release probabilities across buffering conditions (Fig. 8*G*). Taken together, these results indicate that IHCs have a physiological buffering capacity, similar to that of 2 mM BAPTA, contributing to the control of Ca^{2+} diffusion during synaptic activation.

To confirm limited Ca^{2+} spread during efferent activation in a high Ca^{2+} buffering scenario, imaging experiments were performed using 2 mM BAPTA and a stimulating paradigm similar

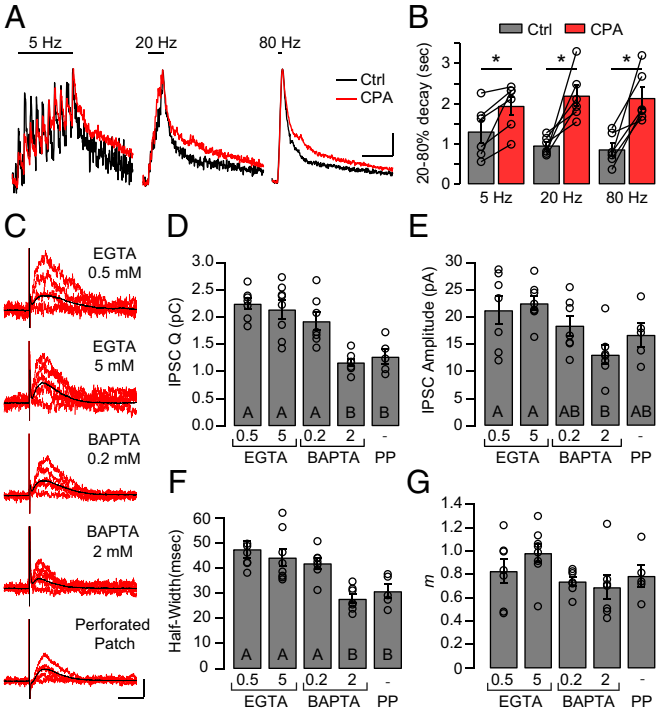

Fig. 8. Cisternal Ca^{2+}-ATPases and high intracellular Ca^{2+} buffering shape electrically evoked IPSCs. (*A*) IHCs were loaded with the fluorescent Ca^{2+} indicator Fluo-4 (400 μM) and EGTA (500 μM), and 10-stimuli trains at 5, 20, and 80 Hz were applied to efferent fibers. Ca^{2+} transients were imaged during stimulation before (black traces) and after incubation with the cisternal Ca^{2+}-ATPase inhibitor CPA (5 μM) (red traces). (Scale bars: 1 s, 0.2 normalized ΔF.) (*B*) Decay kinetics of Ca^{2+} transients in *A*, computed as the τ_{decay} between 20% and 80% of the response peak. Kruskal–Wallis test, $P > 0.05$. Ctrl, control. (*C*) Representative traces of eIPSCs recorded at $V_h = -40$ mV in IHCs in whole-cell mode, using different Ca^{2+} buffering conditions, and in the perforated-patch (PP) configuration. Black traces represent the average of multiple repetitions of stimulation in a given cell. (Scale bars: 50 ms, 20 pA.) The accumulated charge (Q) (*D*), amplitude (*E*), and HW (*F*) in each buffering condition are shown. (*D*) Q: 2.2 ± 0.1 pC in 0.5 mM EGTA ($n = 7$), 2.1 ± 0.2 pC in 5 mM EGTA ($n = 8$), 1.9 ± 0.2 pC in 0.2 mM BAPTA ($n = 7$), 1.2 ± 0.1 pC in 2 mM BAPTA ($n = 7$), and 1.3 ± 0.1 pC ($n = 5$) in PP. (*E*) Amplitude: 21.1 ± 2.6 pA ($n = 7$) in 0.5 mM EGTA, 22.4 ± 1.3 pA ($n = 8$) in 5 mM EGTA, 18.3 ± 1.8 pA ($n = 7$) in 0.2 mM BAPTA, 13.0 ± 1.7 pA ($n = 7$) in 2 mM BAPTA, and 16.6 ± 2.2 pA ($n = 5$) in PP. (*F*) HW: 47 ± 3 ms ($n = 7$) in 0.5 mM EGTA, 44 ± 4 ms ($n = 8$) in 5 mM EGTA, 42 ± 2 ms ($n = 7$) in 0.2 mM BAPTA, 28 ± 2 ms ($n = 7$) in 2 mM BAPTA, and 31 ± 3 ms ($n = 5$) in PP. Different letters indicate statistically significant differences between groups. Kruskal–Wallis test, $P < 0.05$. (*G*) m determined by the failures method: 0.83 ± 0.11 in 0.5 mM EGTA ($n = 7$), 0.98 ± 0. 08 in 5 mM EGTA ($n = 8$ cells), 0.74 ± 0.04 in 0.2 mM BAPTA ($n = 7$), 0.69 ± 0.10 in 2 mM BAPTA ($n = 7$), and 0.79 ± 0.09 in PP conditions ($n = 5$). No significant differences were found.

to the one used in Fig. 4. As shown in Fig. S7, efferent shock trains at 5, 20, and 80 Hz were applied for 3 s and synaptic responses were recorded on the IHC. Maximal fluorescence values were three- to fivefold smaller than those obtained in 0.5 mM EGTA (Fig. 4). The amplitude of the fluorescence signals showed a good correlation with the integral of the electrophysiological responses (Spearman correlation, $P < 0.0001$) and represented a different set of data compared with that obtained using 0.5 mM EGTA (F test, $P < 0.0001$) (Fig. S7*E*).

IHC AP Firing Is Modulated by the Efferent Stimulation Rate. Before the onset of hearing, IHCs fire sensory-independent APs (3, 4) and activation of the efferent system inhibits this firing (10, 20, 26, 32). To assess the minimal amount of efferent inhibition required to modulate AP firing, efferent axons were electrically stimulated at frequencies between 2 and 80 Hz while recording from IHCs in the current-clamp mode (Fig. 7). In the excised organ of Corti preparation from P9–P10 mice, IHCs typically do not fire spontaneously but require a small current injection (10–30 pA) to trigger APs (40). As shown in Fig. 7 *A* and *B*, in the absence of inhibition, IHCs fired steadily at 3.8 ± 0.3 Hz (n = 9 cells). Efferent stimulation produced a strong reduction in firing rate compared with the prestimulation period at 10 Hz (78.7 ± 11.8%, $n = 8$ cells), with a maximal effect at 20 and 80 Hz (91.5 ± 4.9 and 98.7 ± 1.3 reduction, respectively; $n = 8$ cells) (Friedman's test, $P < 0.01$) (Fig. 7*B*). In contrast, 2- and 5-Hz efferent stimulation did not produce a significant reduction in the firing rate (Friedman's test, $P > 0.05$). In the same group of cells, voltage-clamp recordings were also performed to evaluate the integral of the ensemble synaptic response during the 3-s electrical stimulation: 2 Hz = 7.1 ± 2.8 pC, 5 Hz = 17.5 ± 2.0 pC, 10 Hz = 71.1 ± 6.3 pC, 20 Hz = 208.7 ± 30.4 pC, 80 Hz = 161.7 ± 36.5 pC (Friedman's test, $P < 0.05$) (Fig. 7 *C* and *D*).

This observation provides a lower bound estimate for the activation rate of the MOC system during development and suggests that a modest near-20-Hz stimulation rate of efferent fibers is sufficient to produce strong, near-maximal inhibition of IHC firing.

Discussion

This study provides functional and morphological evidence for the presence of multiple afferent and efferent synaptic contacts on prehearing IHCs. Most interestingly, these antagonistic Ca^{2+}-mediated synapses were intertwined and closely positioned. The juxtaposition of Ca^{2+}-mediated efferent and afferent synapses within a compact IHC raises the question of whether these can be functionally independent signals. The present results show that efferent synaptic Ca^{2+} influx is tightly regulated to prevent Ca^{2+}-induced glutamate release from IHC ribbon synapses and activation of afferent fibers under physiological conditions. Compartmentalization of Ca^{2+} signals guarantees that efferent fibers contacting IHCs play a solely inhibitory role during the critical developmental period of the auditory system. This supports the hypothesis that efferent inhibition imposes a characteristic pattern onto IHC glutamate release required for the correct development of the auditory system (7, 41).

Efferent Ca^{2+} Entry and Synapse Location. Ca^{2+} imaging techniques combined with electrophysiological recordings revealed the entry of Ca^{2+} through α9α10 nAChRs during discrete synaptic events, and its dynamics during repetitive electrical stimulation. High stimulation frequencies resulted in robust and homogenous cytoplasmic Ca^{2+} signals that might have reached ribbon synapse sites to trigger afferent glutamate release.

To better understand the relative position of efferent-to-afferent synapses within a cell, Ca^{2+} imaging and EM reconstructions were carried out in single IHCs. The total number of synaptic contacts determined through EM techniques was higher than those observed in Ca^{2+} imaging experiments. This difference may stem from multiple sources: (*i*) the higher spatial resolution of EM microscopy that could distinguish closely positioned synapses not resolvable under light microscopy (as indicated in *Results*, a high proportion of afferent synapses are located at <1 μm from the next nearest afferent, similar to what was observed for efferent-to-efferent separation); (*ii*) some morphologically identified synapses might not be functional; and, finally, (*iii*) electrical stimulation might not activate all available fibers of MOC neurons. However, it is important to note that, irrespective of the total number of synapses, the intertwined disposition and close proximity between afferent and efferent synapses observed in both EM and functional imaging were striking and in accordance with previously estimated values (42, 43).

Recordings performed in afferent boutons showed that despite the intimate positioning and high-frequency stimulation, efferent synaptic activity failed to evoke the release of glutamate onto afferent terminals in all experiments but one. It should be noted that these experiments were performed in the presence of isradipine to limit Ca^{2+} influx through VGCC (isradipine was not required in the experiments in Fig. 5, given the robust and nonstochastic inhibition produced on IHCs by ACh applications, in contrast to the weaker and stochastic nature of synaptic inhibition). Isradipine produced a ninefold increase in the release probability of efferent synapses, most likely through the inhibition of presynaptic L-type channels that ordinarily contribute to BK channel activation on efferent fibers (36). Thus, despite the fact that under these experimental conditions, the Ca^{2+} load through α9α10 is exacerbated, synaptic cross-talk was only observed in one of six stimulation protocols at 80 Hz. In addition, strong synaptic depression was observed during the 3-s shock trains, indicating that the stimulation paradigm reaches near-maximum effect and that extending the stimulation would not produce larger responses. Only prolonged nonphysiological applications of saturating ACh concentrations were able to overwhelm Ca^{2+} diffusion and uptake restrictions, saturate strong intracellular buffering, and evoke glutamate release.

As a whole, the present studies provide functional evidence for the absence of efferent-to-afferent cross-talk during physiological synaptic activity when the IHC intracellular milieu remains unperturbed. This implies that opposing Ca^{2+} signals operate independently, increasing the information capacity of signaling within the developing IHC. Consequently, efficient cellular mechanisms are proposed to secure Ca^{2+} signal compartmentalization so that efferent cholinergic synaptic activity retains its inhibitory nature. It should be mentioned that this study was carried out on an ex vivo preparation of the organ of Corti of rats and mice at room temperature; thus, results may differ from an in vivo situation.

Mechanism of Cross-Talk Prevention. Ca^{2+} signal compartmentalization enhances the computational power of individual cells (44, 45). In the case of dendritic spines, compartmentalization relies on precise membrane channel location, Ca^{2+} buffering, spine morphology, and intracellular Ca^{2+} stores (46–48) to create an isolated signaling compartment in which one synapse can operate independent of the machinery associated with a neighboring synapse (47). Here, we show that fast, millimolar Ca^{2+} buffering, subsynaptic cisterns contributing to Ca^{2+} uptake and low efferent firing rates underlie the lack of Ca^{2+} cross-talk from efferent to afferent synapses.

EM reconstructions revealed the widespread presence of near-membrane cisterns on efferent synaptic sites, similar to those described in the outer hair cell (OHC) (43, 49–51). Interestingly, these postsynaptic cisterns were precisely associated with presynaptic efferent active zones. The near-membrane cistern would limit Ca^{2+} diffusion during efferent activity, resulting in an

enhanced and localized increase in Ca^{2+} concentration. Such effects have been shown in simulations of Ca^{2+} dynamics in the cytoplasmic space between cisterns and the plasmatic membrane of both hair cells and nonhair cells (52, 53). Additionally, postsynaptic cisterns can operate as Ca^{2+} sinks, as indicated by the results in Fig. 8, producing a briefer decay in transients triggered by moderately short stimuli. OHC cisterns have been proposed to serve as a store for the Ca^{2+}-induced Ca^{2+}-release mechanism during prolonged ACh activation (54–56). However, it is likely that Ca^{2+} influx through the highly permeable α9α10 nAChR (23, 24) is necessary and sufficient to gate the closely positioned SK2 channels as proposed previously (25, 28). The present perforated patch-clamp recordings (which preserve endogenous buffers) demonstrate that the IHC buffer capacity allows activation of SK2 channels but prevents extensive Ca^{2+} spread during synaptic activation of α9α10 nAChRs. Under these conditions, the amplitude and kinetics of the evoked IPSCs resembled those observed in the presence of millimolar concentrations of the fast Ca^{2+}-binding buffer BAPTA as previously reported (28). Strong Ca^{2+} buffering is probably due to the presence of calbindin-D28k, an abundant protein in prehearing IHCs that exhibits fast Ca^{2+}-binding kinetics (57, 58).

One cannot disregard the possibility that efferent Ca^{2+} influx might have some longer term modulatory impact on afferent synaptic function. The release probability of glutamate-filled vesicles is modulated by a number of Ca^{2+}-dependent mechanisms such as VGCC Ca^{2+}-dependent inactivation (59, 60), vesicle recruitment to the release site (61), and short-term facilitation (62, 63). Moreover, the reverse afferent to efferent Ca^{2+} cross-talk cannot be excluded and was not investigated in the current study. It has been reported that Ca^{2+} entering through VGCCs can activate SK2 channels, which may contribute to the repetitive AP waveform in prehearing IHCs (28, 64). Additionally, an increased cytoplasmic Ca^{2+} concentration (e.g., due to influx through VGCCs) might have a loading effect on the efferent postsynaptic cistern, resulting in a positive modulation of ACh responses (55). These possibilities of afferent-to-efferent cross-talk are strengthened by the presence of extrasynaptic VGCCs, producing a widespread distribution of Ca^{2+} within the developing IHC (65).

In summary, the immature IHC relies on Ca^{2+} buffering and the effect of the postsynaptic cistern as a diffusion barrier, and also a Ca^{2+} sink, to prevent efferent Ca^{2+} from reaching afferent release sites. Most importantly, tight regulation of isolated Ca^{2+} microdomains ensures that efferent innervation solely serves to inhibit the spontaneous firing activity of IHCs and cochlear afferents during development.

Developmental Spontaneous Firing Activity. Spontaneous electrical activity in the developing auditory pathway is crucial for its maturation and the correct establishment of tonotopic maps (7, 66, 67). This activity arises in the cochlea and presents a very specific temporal pattern (5, 7, 9, 10). The ablation of the efferent/cholinergic system during development leads to a modified pattern of activity, and ultimately, to altered establishment of synaptic connections (7) and hearing deficits (8, 29). Although critical, the contribution of the MOC system to the temporal structure of the spiking pattern represents changes in the millisecond range (7, 41). Data in Fig. 7 indicate that this fine modulation requires a low efferent activation rate, in the range of a few hertz. If stimulated at higher rates, the MOC system would completely inhibit IHC AP firing. A fundamental implication of this low firing rate is a reduced IHC Ca^{2+} load through the highly Ca^{2+}-permeable α9α10 nAChRs. This would work in concert with the compartmentalization mechanisms to ensure a tight control of efferent postsynaptic Ca^{2+} spread.

Methods

Electrophysiological recordings were performed on IHCs and boutons of auditory nerve neurons from P9–P11 mouse or rat cochleae (following guidelines of INGEBI and The Johns Hopkins University Institutional Animal Care and Use Committees). Ca^{2+} indicator dyes were introduced into the IHCs through a patch pipette and then imaged using wide-field or swept-field confocal microscopy. Electrical stimulation of efferent axons was applied to evoke synaptic activity. Drugs were introduced through the bath perfusion system. Ultrathin serial section EM was carried out on midturn cochlear segments from two P9 rats. A full description of methods used is provided in *SI Methods*.

ACKNOWLEDGMENTS. We thank Michael J. Caterina for providing access to the swept-field confocal microscope (supported by the Neurosurgery Pain Research Institute at Johns Hopkins), David Zenisek for the gift of the RIBEYE-binding peptide, Carlos Valverde for providing valuable reagents and John Dempster for WinWCP software. We also thank Claudia Gatto and Nicolás Gilio for excellent technical assistance and Régis Nouvian for advice on perforated-patch recordings. This study was funded by Proyecto de Investigación Científica y Tecnológica (PICT) Grant 2016-2155 (to J.D.G.), PICT Grant 2015-0919 (to A.B.E.), National Institute on Deafness and Other Communication Disorders Grants R01 DC001508 (to P.A.F. and A.B.E.) and R01 DC015309 (to P.A.F.), and Firca-NIH Grant 1R03TW009403-01 [to J.D.G. and Elisabeth Glowatzki (principal investigator)]. M.J.M. is the recipient of a "Bec.Ar" Presidential fellowship supported by the Argentinian government.

1. Puel JL, Uziel A (1987) Correlative development of cochlear action potential sensitivity, latency, and frequency selectivity. *Brain Res* 465:179–188.
2. Geal-Dor M, Freeman S, Li G, Sohmer H (1993) Development of hearing in neonatal rats: Air and bone conducted ABR thresholds. *Hear Res* 69:236–242.
3. Marcotti W, Johnson SL, Rüsch A, Kros CJ (2003) Sodium and calcium currents shape action potentials in immature mouse inner hair cells. *J Physiol* 552: 743–761.
4. Kros CJ, Ruppersberg JP, Rüsch A (1998) Expression of a potassium current in inner hair cells during development of hearing in mice. *Nature* 394:281–284.
5. Tritsch NX, et al. (2010) Calcium action potentials in hair cells pattern auditory neuron activity before hearing onset. *Nat Neurosci* 13:1050–1052.
6. Kandler K, Clause A, Noh J (2009) Tonotopic reorganization of developing auditory brainstem circuits. *Nat Neurosci* 12:711–717.
7. Clause A, et al. (2014) The precise temporal pattern of prehearing spontaneous activity is necessary for tonotopic map refinement. *Neuron* 82:822–835.
8. Clause A, Lauer AM, Kandler K (2017) Mice lacking the alpha9 subunit of the nicotinic acetylcholine receptor exhibit deficits in frequency difference limens and sound localization. *Front Cell Neurosci* 11:167.
9. Tritsch NX, Yi E, Gale JE, Glowatzki E, Bergles DE (2007) The origin of spontaneous activity in the developing auditory system. *Nature* 450:50–55.
10. Johnson SL, et al. (2011) Position-dependent patterning of spontaneous action potentials in immature cochlear inner hair cells. *Nat Neurosci* 14:711–717.
11. Johnson SL, Kennedy HJ, Holley MC, Fettiplace R, Marcotti W (2012) The resting transducer current drives spontaneous activity in prehearing mammalian cochlear inner hair cells. *J Neurosci* 32:10479–10483.
12. Johnson SL, et al. (2016) Connexin-mediated signalling in non-sensory cells is crucial for the development of sensory inner hair cells in the mouse cochlea. *J Neurosci* 37:258–268.
13. Wang HC, et al. (2015) Spontaneous activity of cochlear hair cells triggered by fluid secretion mechanism in adjacent support cells. *Cell* 163:1348–1359.
14. Liberman MC (1980) Morphological differences among radial afferent fibers in the cat cochlea: An electron-microscopic study of serial sections. *Hear Res* 3:45–63.
15. Liberman M (1982) Single-neuron labeling in the cat auditory nerve. *Science* 216: 1239–1241.
16. Beutner D, Moser T (2001) The presynaptic function of mouse cochlear inner hair cells during development of hearing. *J Neurosci* 21:4593–4599.
17. Glowatzki E, Fuchs PA (2002) Transmitter release at the hair cell ribbon synapse. *Nat Neurosci* 5:147–154.
18. Simmons DD, Mansdorf NB, Kim JH (1996) Olivocochlear innervation of inner and outer hair cells during postnatal maturation: Evidence for a waiting period. *J Comp Neurol* 370:551–562.
19. Guinan JJ, Jr (2006) Olivocochlear efferents: Anatomy, physiology, function, and the measurement of efferent effects in humans. *Ear Hear* 27:589–607.
20. Glowatzki E, Fuchs PA (2000) Cholinergic synaptic inhibition of inner hair cells in the neonatal mammalian cochlea. *Science* 288:2366–2368.
21. Elgoyhen AB, Johnson DS, Boulter J, Vetter DE, Heinemann S (1994) Alpha 9: An acetylcholine receptor with novel pharmacological properties expressed in rat cochlear hair cells. *Cell* 79:705–715.
22. Elgoyhen AB, et al. (2001) Alpha10: A determinant of nicotinic cholinergic receptor function in mammalian vestibular and cochlear mechanosensory hair cells. *Proc Natl Acad Sci USA* 98:3501–3506.

23. Gómez-Casati ME, Fuchs PA, Elgoyhen AB, Katz E (2005) Biophysical and pharmacological characterization of nicotinic cholinergic receptors in rat cochlear inner hair cells. *J Physiol* 566:103–118.
24. Weisstaub N, Vetter DE, Elgoyhen AB, Katz E (2002) The alpha9alpha10 nicotinic acetylcholine receptor is permeable to and is modulated by divalent cations. *Hear Res* 167:122–135.
25. Oliver D, et al. (2000) Gating of Ca2+-activated K+ channels controls fast inhibitory synaptic transmission at auditory outer hair cells. *Neuron* 26:595–601.
26. Sendin G, Bourien J, Rassendren F, Puel J-L, Nouvian R (2014) Spatiotemporal pattern of action potential firing in developing inner hair cells of the mouse cochlea. *Proc Natl Acad Sci USA* 111:1999–2004.
27. Katz E, et al. (2004) Developmental regulation of nicotinic synapses on cochlear inner hair cells. *J Neurosci* 24:7814–7820.
28. Marcotti W, Johnson SL, Kros CJ (2004) A transiently expressed SK current sustains and modulates action potential activity in immature mouse inner hair cells. *J Physiol* 560: 691–708.
29. Walsh EJ, McGee J, McFadden SL, Liberman MC (1998) Long-term effects of sectioning the olivocochlear bundle in neonatal cats. *J Neurosci* 18:3859–3869.
30. Frank T, Khimich D, Neef A, Moser T (2009) Mechanisms contributing to synaptic Ca2+ signals and their heterogeneity in hair cells. *Proc Natl Acad Sci USA* 106:4483–4488.
31. Francis AA, Mehta B, Zenisek D (2011) Development of new peptide-based tools for studying synaptic ribbon function. *J Neurophysiol* 106:1028–1037.
32. Goutman JD, Fuchs PA, Glowatzki E (2005) Facilitating efferent inhibition of inner hair cells in the cochlea of the neonatal rat. *J Physiol* 566:49–59.
33. Evans MG, Lagostena L, Darbon P, Mammano F (2000) Cholinergic control of membrane conductance and intracellular free Ca2+ in outer hair cells of the Guinea pig cochlea. *Cell Calcium* 28:195–203.
34. Shigemoto T, Ohmori H (1990) Muscarinic agonists and ATP increase the intracellular Ca2+ concentration in chick cochlear hair cells. *J Physiol* 420:127–148.
35. Brandt A, Striessnig J, Moser T (2003) CaV1.3 channels are essential for development and presynaptic activity of cochlear inner hair cells. *J Neurosci* 23:10832–10840.
36. Zorrilla de San Martín J, Pyott S, Ballestero J, Katz E (2010) Ca(2+) and Ca(2+)-activated K(+) channels that support and modulate transmitter release at the olivocochlear efferent-inner hair cell synapse. *J Neurosci* 30:12157–12167.
37. Goeger DE, Riley RT, Dorner JW, Cole RJ (1988) Cyclopiazonic acid inhibition of the Ca2+-transport ATPase in rat skeletal muscle sarcoplasmic reticulum vesicles. *Biochem Pharmacol* 37:978–981.
38. Fuchs PA, Murrow BW (1992) A novel cholinergic receptor mediates inhibition of chick cochlear hair cells. *Proc Biol Sci* 248:35–40.
39. Del Castillo J, Katz B (1954) Quantal components of the end-plate potential. *J Physiol* 124:560–573.
40. Marcotti W, Johnson SL, Holley MC, Kros CJ (2003) Developmental changes in the expression of potassium currents of embryonic, neonatal and mature mouse inner hair cells. *J Physiol* 548:383–400.
41. Walsh EJ, McGee J (1997) Does activity in the olivocochlear bundle affect development of the auditory periphery? *International Symposium on Diversity in Auditory Mechanics*, eds Lewis ER, et al. (World Scientific, Singapore), pp 376–385.
42. Ye Z, Goutman JD, Pyott SJ, Glowatzki E (2017) mGluR1 enhances efferent inhibition of inner hair cells in the developing rat cochlea. *J Physiol* 595:3483–3495.
43. Bruce LL, Christensen MA, Warr WB (2000) Postnatal development of efferent synapses in the rat cochlea. *J Comp Neurol* 423:532–548.
44. Lee KFHH, Soares C, Thivierge JP, Béïque J-CC (2016) Correlated synaptic inputs drive dendritic calcium amplification and cooperative plasticity during clustered synapse development. *Neuron* 89:784–799.
45. Augustine GJ, Santamaria F, Tanaka K (2003) Local calcium signaling in neurons. *Neuron* 40:331–346.
46. Bootman MD, Lipp P, Berridge MJ (2001) The organisation and functions of local Ca(2+) signals. *J Cell Sci* 114:2213–2222.
47. Higley MJ, Sabatini BL (2012) Calcium signaling in dendritic spines. *Cold Spring Harb Perspect Biol* 4:a005686.
48. Yuste R, Majewska A, Holthoff K (2000) From form to function: Calcium compartmentalization in dendritic spines. *Nat Neurosci* 3:653–659.
49. Saito K (1983) Fine structure of the sensory epithelium of Guinea-pig organ of Corti: Subsurface cisternae and lamellar bodies in the outer hair cells. *Cell Tissue Res* 229: 467–481.
50. Shnerson A, Devigne C, Pujol R (1981) Age-related changes in the C57BL/6J mouse cochlea. II. Ultrastructural findings. *Brain Res* 254:77–88.
51. Fuchs PA, Lehar M, Hiel H (2014) Ultrastructure of cisternal synapses on outer hair cells of the mouse cochlea. *J Comp Neurol* 522:717–729.
52. Hong D, Jaron D, Buerk DG, Barbee KA (2008) Transport-dependent calcium signaling in spatially segregated cellular caveolar domains. *Am J Physiol Cell Physiol* 294: C856–C866.
53. Martin AR, Fuchs PA (1992) The dependence of calcium-activated potassium currents on membrane potential. *Proc Biol Sci* 250:71–76.
54. Fuchs PA (2014) A 'calcium capacitor' shapes cholinergic inhibition of cochlear hair cells. *J Physiol* 592:3393–3401.
55. Im GJ, Moskowitz HS, Lehar M, Hiel H, Fuchs PA (2014) Synaptic calcium regulation in hair cells of the chicken basilar papilla. *J Neurosci* 34:16688–16697.
56. Lioudyno M, et al. (2004) A "synaptoplasmic cistern" mediates rapid inhibition of cochlear hair cells. *J Neurosci* 24:11160–11164.
57. Nägerl UV, Novo D, Mody I, Vergara JL (2000) Binding kinetics of calbindin-D(28k) determined by flash photolysis of caged Ca(2+). *Biophys J* 79:3009–3018.
58. Hackney CM, Mahendrasingam S, Penn A, Fettiplace R (2005) The concentrations of calcium buffering proteins in mammalian cochlear hair cells. *J Neurosci* 25:7867–7875.
59. Cui G, et al. (2007) Ca2+-binding proteins tune Ca2+-feedback to Cav1.3 channels in mouse auditory hair cells. *J Physiol* 585:791–803.
60. Grant L, Fuchs P (2008) Calcium- and calmodulin-dependent inactivation of calcium channels in inner hair cells of the rat cochlea. *J Neurophysiol* 99:2183–2193.
61. Schnee ME, Santos-Sacchi J, Castellano-Muñoz M, Kong JH, Ricci AJ (2011) Calcium-dependent synaptic vesicle trafficking underlies indefatigable release at the hair cell afferent fiber synapse. *Neuron* 70:326–338.
62. Goutman JD, Glowatzki E (2011) Short-term facilitation modulates size and timing of the synaptic response at the inner hair cell ribbon synapse. *J Neurosci* 31:7974–7981.
63. Cho S, Li G-L, von Gersdorff H (2011) Recovery from short-term depression and facilitation is ultrafast and Ca2+ dependent at auditory hair cell synapses. *J Neurosci* 31: 5682–5692.
64. Kong J-H, Adelman JP, Fuchs PA (2008) Expression of the SK2 calcium-activated potassium channel is required for cholinergic function in mouse cochlear hair cells. *J Physiol* 586:5471–5485.
65. Wong AB, et al. (2014) Developmental refinement of hair cell synapses tightens the coupling of Ca2+ influx to exocytosis. *EMBO J* 33:247–264.
66. Erazo-Fischer E, Striessnig J, Taschenberger H (2007) The role of physiological afferent nerve activity during in vivo maturation of the calyx of Held synapse. *J Neurosci* 27: 1725–1737.
67. Leao RN, et al. (2006) Topographic organization in the auditory brainstem of juvenile mice is disrupted in congenital deafness. *J Physiol* 571:563–578.
68. Zenisek D, Horst NK, Merrifield C, Sterling P, Matthews G (2004) Visualizing synaptic ribbons in the living cell. *J Neurosci* 24:9752–9759.
69. Kennedy HJ (2002) Intracellular calcium regulation in inner hair cells from neonatal mice. *Cell Calcium* 31:127–136.
70. Dean KM, Roudot P, Welf ES, Danuser G, Fiolka R (2015) Deconvolution-free subcellular imaging with axially swept light sheet microscopy. *Biophys J* 108:2807–2815.
71. Sage D, Neumann FR, Hediger F, Gasser SM, Unser M (2005) Automatic tracking of individual fluorescence particles: Application to the study of chromosome dynamics. *IEEE Trans Image Process* 14:1372–1383.
72. Ollion J, Cochennec J, Loll F, Escudé C, Boudier T (2013) TANGO: A generic tool for high-throughput 3D image analysis for studying nuclear organization. *Bioinformatics* 29:1840–1841.
73. Fiala JC (2005) Reconstruct: A free editor for serial section microscopy. *J Microsc* 218: 52–61.